Research Square

Preprints are preliminary reports that have not undergone peer review.
They should not be considered conclusive, used to inform clinical practice,
or referenced by the media as validated information.

A Miniaturized Mid-Infrared Spectrometer Enabled by Hybrid Encoding of q-BIC Thermal Emitters with Uncooled Imaging

Qin Chen

chenqin2018@jnu.edu.cn

Jinan University https://orcid.org/0000-0001-8972-2568

long wen

Jinan University https://orcid.org/0000-0002-8796-4376

Qinke Liu

Jinan University

Yuyang Wang

Jinan University

Zikun Xia

Jinan University

Yiyao Lu

Jinan University

Yucong Huang

Jinan University

Yang Zhang

Jinan University

Baojun Li

1 https://orcid.org/0000-0002-7481-7780

Article

Keywords: Thermal radiation, q-BIC, Spectrometer, Mid-infrared spectroscopy

Posted Date: September 21st, 2026

DOI: https://doi.org/10.21203/rs.3.rs-10870425/v1

License: This work is licensed under a Creative Commons Attribution 4.0 International License.
Read Full License

Additional Declarations: There is no conflict of interest

A Miniaturized Mid-Infrared Spectrometer Enabled by Hybrid Encoding of *q*-BIC Thermal Emitters with Uncooled Imaging

Long Wen[#], Qinke Liu[#], Yuyang Wang, Zikun Xia, Yiyao Lu, Yucong Huang, Yang Zhang*, Qin Chen* and Baojun Li*

Jinan University, College of Physics & Optoelectronic Engineering, Institute of Nanophotonics, Guangdong Provincial Key Laboratory of Nanophotonic Manipulation, Guangzhou, China

[#]*These authors contributed equally to this work*

[*]*Correspondence*: yangzhang@jnu.edu.cn; chenqin2018@jnu.edu.cn; baojunli@jnu.edu.cn

Abstract

Mid-infrared molecular fingerprint spectroscopy is indispensable for chemical identification and materials analysis. Yet its deployment beyond laboratory settings remains severely constrained by the inherent limitations of conventional technologies—FTIR instruments are bulky and expensive, NDIR suffers from poor spectral resolution, and TDLAS offers only a narrow tuning range. Here, we propose and experimentally demonstrate a hybrid spectral encoding scheme based on quasi-bound states in the continuum (q-BIC) metasurfaces. By leveraging the thermo-optic effect of germanium, our scheme synergistically integrates geometrically tailored emitter channels with thermally tunable spectral states. This mixed tuning strategy generates 40 distinct narrowband channels spanning the 7.5–10 μm range from only eight physical channels. The resulting spectrally encoded signals are captured by an uncooled thermal camera, forming a compact and cost-effective spectrometer system. Combined with thermal background subtraction and compressed-sensing reconstruction, our system performs the decoding from thermal images to spectra, thereby achieving a spectral resolution below 100 nm and enabling multiple practical mid-infrared analysis tasks, including material sorting, concentration quantification, and imidization process monitoring. Notably, the hybrid encoding strategy is inherently scalable to densely packed spectral imaging arrays, offering a promising route toward high-resolution spatial–spectral molecular sensing within a truly miniaturized form factor.

Keywords: Thermal radiation, *q*-BIC, Spectrometer, Mid-infrared spectroscopy

Introduction

Mid-infrared (MIR) molecular fingerprint spectroscopy, spanning the 2.5–20 μm wavelength range, provides direct access to the characteristic rotational–vibrational absorption signatures of most organic and inorganic molecules[1], making it an indispensable tool for chemical identification, environmental monitoring, biomedical diagnostics, and industrial process control[2]. Yet despite this fundamental importance, the vast majority of MIR spectroscopic analyses remain confined to well-equipped laboratory settings. The prevailing workhorse—Fourier-transform infrared (FTIR) spectrometry[3]—offers exceptional spectral resolution and signal-to-noise ratio, but at the cost of bulky optical benches, precision moving components, and often cryogenic cooling. Alternative technologies such as non-dispersive infrared (NDIR)[4] are compact but suffer from intrinsically poor spectral discrimination, while tunable diode laser absorption spectroscopy (TDLAS)[5] provides only limited scanning ranges and is typically locked to specific gas-phase transitions. These complementary yet individually incomplete shortcomings collectively prevent the translation of MIR spectroscopy from centralized labs into portable, cost-effective, and field-deployable formats—an increasingly pressing need across applications ranging from on-site environmental monitoring to point-of-care medical diagnostics and industrial quality assurance[6].

Recent advances in nanophotonics have revolutionized optical manipulation at subwavelength scales, spurring a surge of chip-scale spectrometers and spectral imaging devices in the visible and near-infrared regimes[7-11]. In the MIR band, efforts toward miniaturized spectroscopy have broadly followed two distinct routes[12-19], both operating at the *detection side*—that is, spectral manipulation is performed either in the optical path preceding the detector or directly on the detector focal-plane array. The first route places multi-channel narrowband filters in the optical path preceding the detector[12-15]. This approach, however, demands supplementary optical components such as beam expanders and collimation systems[12-14], which compromise system compactness, while MIR optical components remain prohibitively expensive. The second, more ambitious route integrates MIM (metal–insulator–metal) absorbers directly onto uncooled bolometer pixels, aiming for on-chip spectral detection in a pixel-matched format[16-17]. While conceptually attractive, MIM resonators rely on strongly dissipative plasmonic modes that inherently exhibit ultrabroad linewidths (>1 μm)[16-18], precluding high-resolution spectroscopy. Beyond these individual limitations, both detection-side strategies share two fundamental bottlenecks that are particularly acute in the MIR. First,

conventional imaging optics necessarily deliver signals across a wide angular cone; maintaining filter performance over such angular spread forces designers to adopt intrinsically lossy, angle-tolerant structures, directly sacrificing spectral resolution. Second, and more critically, there exists a severe size mismatch between high-quality-factor (Q) resonant structures and modern MIR bolometer pixels (standard pitch ~12 μm). High-Q resonances require large periodic arrays to suppress edge radiation losses—a condition incompatible with pixel-scale footprints[19]. Conversely, structures that do match the pixel size are predominantly low-Q by nature. Direct integration of absorbers onto suspended bolometer bridges also poses formidable fabrication challenges. Consequently, despite considerable efforts, *detection-side* spectral manipulation has yet to yield a practical, high-resolution MIR spectrometer in a truly compact form.

An entirely different, yet surprisingly less explored, paradigm is to perform spectral manipulation at the *source side*—i.e., engineering the thermal radiation source itself rather than filtering the incoming light[20,21]. Any object above absolute zero emits thermal radiation, but its spectral characteristics are governed by bulk material properties (Planck's law), yielding broad and featureless emission. Metasurfaces offer a powerful means to break this limitation by shaping the emissivity spectrum via structured resonances, enabling spectrally and directionally selective thermal emission with enhanced coherence[22-25]. The pursuit of narrowband thermal emission with high-quality factors has a history spanning nearly two decades, during which various mechanisms have been explored—from surface phonon polaritons in SiC gratings[26-27] and surface waves on metallic gratings[28-29], to multilayer interference structures[30,31] and, more recently, quasi-bound states in the continuum (*q*-BIC) enabled by band folding[32-34]. Yet, it is crucial to recognize that all these demonstrations remain at the stage of principle verification, relying exclusively on FTIR systems equipped with high-sensitivity cryogenic MCT detectors and meticulously shielded against environmental thermal background. Translating these high-Q emitters into a practical, low-cost spectroscopic system has never been achieved, for several deep-seated reasons. The MIR spectral regime is plagued by ubiquitous thermal background radiation—from ambient surroundings, structural reflections, and ohmic losses within the metallic components themselves—which severely degrades signal fidelity. While cryogenic detection can mitigate this issue, it is inherently incompatible with portable applications. Meanwhile, high-Q resonances typically exhibit pronounced angular sensitivity[26-29], demanding stringent collimation and precise alignment that further complicates system design and renders these coherent thermal sources resistant to real-world deployment.

Here, we overcome these long-standing barriers by proposing and experimentally demonstrating a hybrid spectral encoding strategy that exploits the narrowband *q*-BIC thermal emission characteristics in synergy with uncooled thermal imaging. Our approach operates at the source end, circumventing the pixel-scale bottleneck entirely: we combine geometric tuning (eight distinct *q*-BIC emitter channels) with thermo-optic tuning (five temperature states exploiting the large thermo-optic coefficient of germanium) to generate 40 continuously distributed narrowband spectral channels across 7.5–10 μm from merely eight physical devices. These spectrally encoded channels are directly captured by an uncooled thermal camera, and through rigorous background subtraction alongside compressed-sensing (CS) reconstruction, we successfully retrieve the underlying spectra from the thermal images with a spectral resolution below 100 nm. We further validate the practical utility of our miniature spectrometer through three disparate MIR analysis tasks, demonstrating high-fidelity spectral reconstruction and reliable capture of distinct molecular fingerprints—all within a compact, cost-effective architecture.

Results

System Architecture and Hybrid Spectral Encoding Principle

Following the above-described strategy, we construct a miniature MIR spectrometer system based on source-side spectral manipulation, with its architecture schematically illustrated in Fig. 1a. The system comprises three functional modules arranged vertically from bottom to top: a miniature heating stage, a thermally tuned spectral emitter chip, and an uncooled thermal camera. The operating principle centers on two successive physical processes— “heat-to-light” and “light-to-heat” conversion. In the heat-to-light process, the heating stage delivers thermal energy to the emitter chip via thermal conduction, enabling the metasurface source chip to radiate upward with enhanced spectral brightness. Since the chip is positioned at the imaging plane of the thermal camera, the multi-spectral channels can be designed with considerable freedom in both spatial arrangement and physical dimensions, readily accommodating the large periodic arrays required for high-Q resonances. For the light-to-heat process, the emitted narrowband radiation is collected by a germanium lens and projected onto the focal-plane array of the uncooled bolometer, generating thermal images that encode the spectral information. When a target sample is inserted in the optical path, its molecular fingerprint absorption selectively attenuates specific spectral channels according to its characteristic vibrational transitions. This differential absorption produces a distinct temperature contrast pattern across the emitter channels in the thermal image, forming a

material-specific QR-code-like spectral signature that enables direct spectroscopic identification [21]. The entire system operates without cryogenic cooling or bulky optics, offering a compact, low-cost platform for practical MIR spectroscopy.

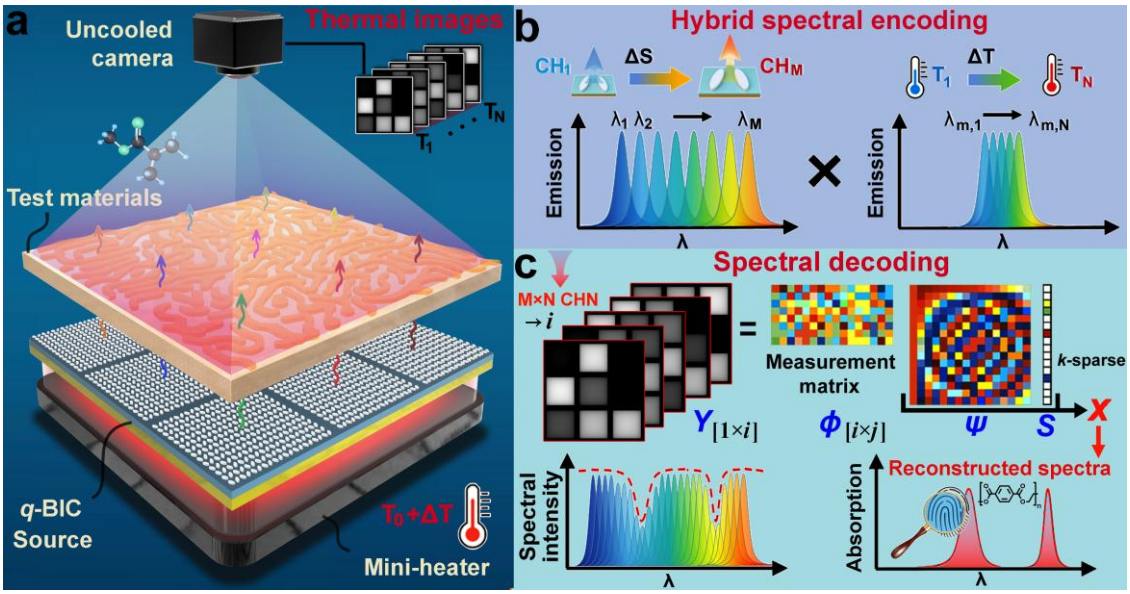


Figure 1. Principle of the miniaturized MIR spectrometer with hybrid spectral encoding. a, System architecture based on source-side spectral manipulation. b, Hybrid encoding combining geometric tuning (M channels) and thermo-optic tuning (N states), expanding the effective channel count to M × N. c, CS reconstruction of the target spectrum X from the thermal readout Y and the measurement matrix Φ.

The performance of a spectrometer based on on-chip spectral manipulation relies on both narrow spectral bandwidth and sufficient channel coverage across the target wavelength range. Here, instead of relying solely on geometric tuning, we introduce a hybrid spectral encoding mechanism that combines geometric tuning with thermo-optic tuning to efficiently multiply the effective spectral channels. As illustrated in Fig. 1b, M geometrically distinct channels are first designed to generate discrete narrowband emissions across the target spectral range. On these geometrically defined channels, we further superimpose N thermo-optic tuning states, each shifting the resonance wavelengths slightly via refractive index modulation. This approach inserts additional spectral channels in the gaps between adjacent geometric peaks, effectively expanding the channel count from M to M × N while requiring only N snapshot measurements. Building on this hybrid encoding scheme, the M × N effective spectral channels are converted by the thermal camera into M × N temperature-coded readout signals. To resolve the fine molecular fingerprint features from these limited measurements—far fewer than the spectral data points required for precise spectroscopic identification—we further incorporate a CS algorithm. As illustrated in Fig. 1c, the transmitted spectrum X of an unknown sample is encoded into the i-dimensional (i = M × N) readout Y through the system response, with each channel carrying distinct absorption information of the material. Prior to measurements, we

construct the spectral response matrix Φ (dimension $i \times j$, with $j \gg i$) by calibrating each encoding channel across the entire wavelength range. This calibration combines the FTIR-measured emission spectra, the camera's spectral responsivity, and both the active thermal emission and multiple background radiation contributions modeled by Planck's law. The final Φ is obtained after rigorous background subtraction; the detailed calibration and reconstruction procedures are provided in the following sections and the Supplementary Information. According to CS theory, if X is sparse in a certain basis Ψ (i.e., $X = \Psi \cdot s$, with s being the sparse coefficient vector), the original spectrum can be accurately reconstructed by solving an ℓ_1-norm optimization problem: $\min\|s\|_1$ subject to $\|Y - \Phi \cdot \Psi \cdot s\|_2 \leq \eta$, where η is a lumped parameter accounting for measurement error, camera noise, and other system imperfections. This decoding approach enables high-fidelity spectral recovery from only i thermal-image readouts, significantly enhancing the reconstruction accuracy and robustness of our miniaturized spectrometer system.

Design and Simulation of *q*-BIC Thermal Emitters

The core of the source-side encoding strategy lies in the ability to generate multiple narrowband thermal emission states with distinct center wavelengths, narrow linewidths, and excellent peak-to-background contrast across the entire target wavelength regime. Among the various approaches to narrowband thermal emission, the *q*-BIC offers a compelling solution: it combines the high-Q nature of a guided-mode resonance with a controlled radiative leakage that can be engineered by symmetry breaking, making it particularly suitable for compact, source-side spectral encoding. To this end, we design a mirror-coupled thermal emitter unit consisting of Ge dual-ellipse resonators, a ZnS spacer layer, and an Au back-reflector with optically thickness (Fig. 2a). The Ge resonators provide strong electric field confinement for the target mode, while the ZnS spacer layer mediates the coupling between the resonators and the optically thick Au back-reflector, which suppresses downward transmission. For this opaque structure, Kirchhoff's law dictates that the spectral emissivity satisfies $\varepsilon = A$, so that resonant absorption directly translates into upward-collectable narrowband thermal radiation.

The targeted narrowband emission arises from band folding of a guided mode and symmetry breaking via rotational perturbation. In the single-ellipse lattice with period p_x, a high-Q guided mode exists at the Brillouin zone boundary $X = \pi/p_x$ but cannot couple to free-space radiation. By adopting a two-ellipse supercell with period $P_x = 2p_x$, this mode is folded to Γ, as shown in the calculated band structure of Fig. 2b (red and blue bands represent the same dispersion before and after folding). In the absence of rotational perturbation, the folded

mode at Γ remains an ideal BIC protected by symmetry. When adjacent ellipses are counter-rotated, the symmetry is broken, the mode acquires radiative leakage, and becomes a *q*-BIC that manifests as a narrowband guided-mode resonance in the far field. The counter-rotation thus simultaneously folds the mode to Γ and opens a radiative channel to free space. Since our spectral encoding relies on thermal imaging, the emitted radiation is collected by a lens over a finite angular range. This imposes a critical requirement on the angular dispersion of the thermal source: the *q*-BIC resonance must remain stable within the collection angle to ensure faithful encoding. Angular-resolved simulations indicate that the target emission peak remains continuous over an incidence angle range of −4° to 4°, with only a gradual shift in resonance wavelength (Fig. 2c). Given the lens focal length of 6.9 mm, an F-number of 1 (entrance pupil diameter of 6.9 mm), and a working distance of 150 mm, the collection half-angle is estimated to be approximately 1.32°. Within this angular range, the maximum resonance drift is about 4 nm, while the peak width and quality factor remain largely stable. This drift is significantly smaller than the wavelength spacing between adjacent encoding states, confirming that the finite collection angle does not compromise the narrowband emission response or the stability of subsequent spectral calibration.

Having established the baseline *q*-BIC unit, we first employ geometric scaling to construct the spatial encoding axis. Keeping all material thicknesses, the counter-rotation configuration, and the rotation angle fixed, we scale the long axis a, short axis b, and in-plane periods Px and Py simultaneously by a scaling factor S. As S increases from 1 to 1.35, the effective optical path of the resonators increases, shifting the resonance continuously toward longer wavelengths while preserving the narrowband spectral line-shape (Fig. 2d). Eight geometric scales thus yield M = 8 spatially distinct channels with staggered baseline resonance wavelengths, providing broad discrete coverage across the target mid-infrared band. Temperature tuning introduces a second dynamic encoding degree of freedom within each geometric channel. As shown in Figure 2e, the electric field of the target mode is predominantly confined within the Ge resonators, making the resonances sensitive to refractive index changes of Ge. The temperature-dependent refractive index is modeled as $n_{Ge}(T, \lambda) = n_{Ge}(T_0, \lambda) + \kappa \cdot (T - T_0)$, where κ is the thermo-optic coefficient of Ge[35]. As the temperature increases from 473 K to 673 K, the resonance wavelength of a representative channel shifts from 8.623 μm to 8.823 μm, corresponding to a total redshift of 200 nm and an average tuning slope of approximately 1 nm·K^{-1}, as shown in Fig. 2f. Across this temperature range, all states maintain narrowband line-shapes, indicating that the thermo-optic effect primarily shifts the resonance position without degrading spectral selectivity. Unlike re-fabricating devices with different

dimensions, temperature tuning provides a repeatable dynamic means of varying the spectral response on the same physical channel. Further details on the simulation setup and parameter sweeps are provided in Supplementary Section S1.

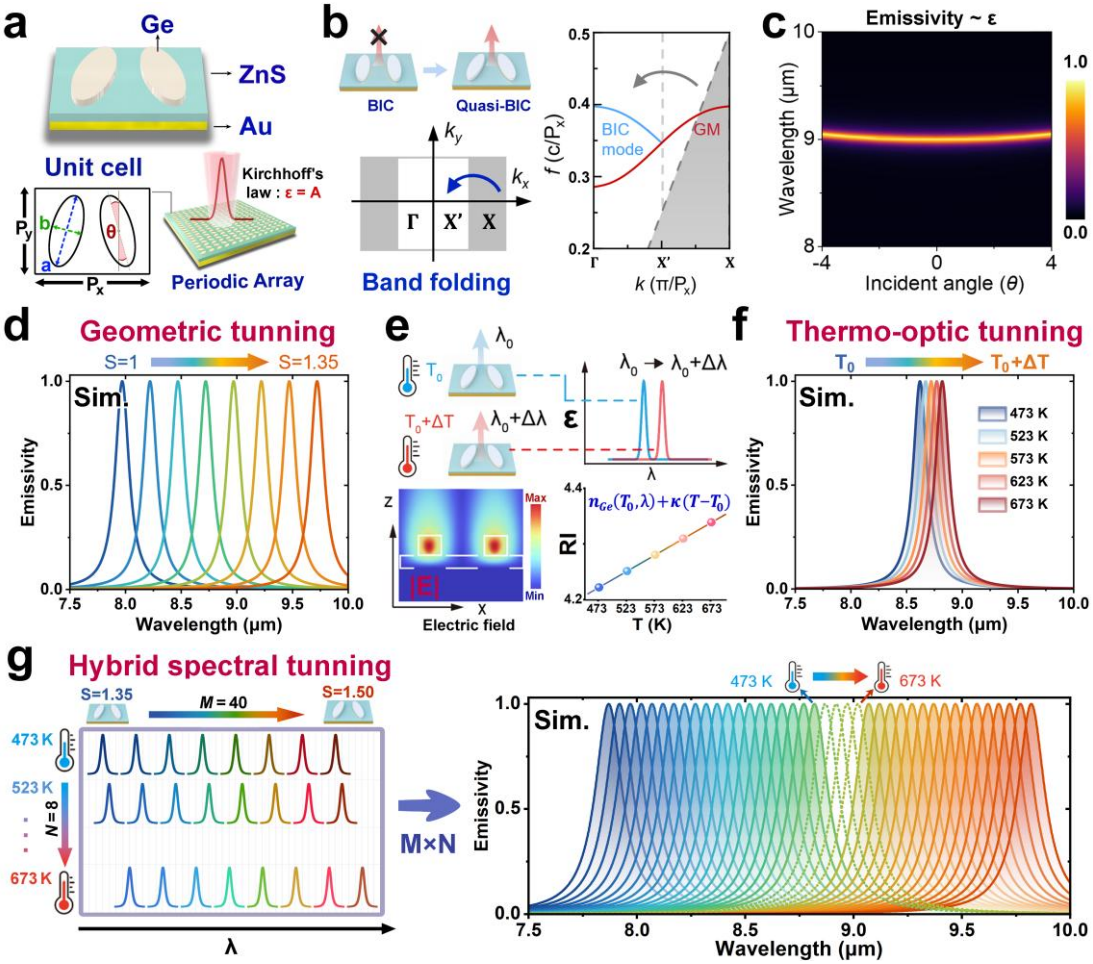


Figure 2. Physical design and hybrid tuning of *q*-BIC thermal emitters. a, Schematic of the mirror-coupled *q*-BIC emitter unit. The geometric parameters (a = 3600 nm, b = 900 nm, Px = 6600 nm, Py = 4050 nm, θ = 15°) are scaled by a factor S to tune the resonance of different spatial channels. The thicknesses of the Ge resonator, ZnS cavity, and Au film are 150, 500, and 700 nm, respectively. b, Illustration of symmetry breaking from BIC to *q*-BIC and Brillouin-zone folding. c. Simulated emission spectra as a function of wavelength and incident angle. d, Simulated emission spectra under different scaling factors. e, Temperature tuning mechanism via the thermo-optic effect of Ge. f, Simulated emission spectra at five temperature states. g, Simulated emission spectra of all hybrid tuning states, combining eight spatial channels and five temperature states to yield 40 distinct narrowband emissions.

Geometric scaling and temperature thus constitute two complementary encoding axes. Geometric scaling determines the baseline resonance positions of each physical channel, providing broad spectral coverage across the target mid-infrared band; temperature tuning further shifts the resonance of each channel after device fabrication, offering finer local spectral sampling without altering the device geometry. By operating the eight spatial channels (M=8) at five discrete temperatures (N=5) the system yields 40 (i = M × N) hybrid states, as illustrated in Figure 2g. Our simulations show that these narrowband emission peaks are interleaved

across the target wavelength range, with the thermo-optically tuned intervals of adjacent channels overlapping to form a denser source-side spectral sampling based on only eight physical emitters. Temperature tuning also provides post-fabrication adjustability for peak alignment and matching of resonances to target absorption bands. Spatial encoding therefore primarily determines the overall spectral coverage, while thermal encoding increases the sampling density within each local band.

Device Fabrication and Experimental Characterization

Having established the design and simulated performance of the q-BIC thermal emitters, we now turn to their experimental characterization. Figure 3a presents SEM images of the fabricated q-BIC multispectral thermal emitter chip. The Ge nanoellipses, defined by electron-beam lithography and hard-mask etching, exhibit smooth sidewalls and well-defined profiles with flat bottom mesa structures. Unlike the visible and near-infrared regimes, the larger feature sizes in the mid-infrared simplify fabrication and provide high tolerance to nanoscale roughness, which remains far below the operating wavelength. Our design is therefore fully compatible with large-area patterning techniques such as stepper lithography and laser direct writing. As shown in the upper-right inset of Fig. 3a, the chip contains eight physically distinct channels (CH_1–CH_8, each 3 mm × 3 mm) corresponding to the eight geometric scaling factors in Fig. 2d, alongside a reference region (ZnS/Au area, CH_r) consisting of an unpatterned ZnS/Au film without Ge resonators, serving as a background reference for subsequent subtraction. Detailed fabrication procedures are provided in Methods and Supplementary Section S2.

To construct the measurement matrix for the CS algorithm, we characterized the thermal emission of the eight channels at five temperatures from 473 K to 673 K using a homebuilt FTIR-based micro-spectral system (see Supplementary S3). The emission signal from each q-BIC channel was collected through a pinhole, collimated by an off-axis parabolic mirror, and coupled into an FTIR spectrometer equipped with a liquid-nitrogen-cooled MCT detector. Absolute emissivity was obtained by referencing against a graphite sample (emissivity >99%) under identical heating conditions:

$$\varepsilon_{CH_i}(\lambda) = \frac{L_{CH_i}(\lambda)}{L_{BB}(\lambda)}$$

where $L_{CH_i}(\lambda)$ and $L_{BB}(\lambda)$ are the measured spectral radiance of the i-th channel and the blackbody reference, respectively, under the same optical path and collection conditions. As shown in Fig. 3b, at 573 K, all eight channels exhibit distinct narrowband emission peaks spanning 7.5–10 μm with nearly equal spacing, in excellent agreement with the simulated peak

positions (see Fig. 2g). Temperature tuning further provides repeatable peak shifts within each spatial channel. Taking CH_4 as a representative example, the resonance wavelength continuously shifts from 8.54 μm to 8.75 μm as the temperature increases from 473 K to 673 K, as shown in Figure 3c. The tuning response across the five temperature states is approximately linear. Across the entire temperature range, the spectral linewidth remains largely unchanged, confirming that our thermo-optic tuning strategy preserves spectral selectivity while effectively expanding the channel capacity.

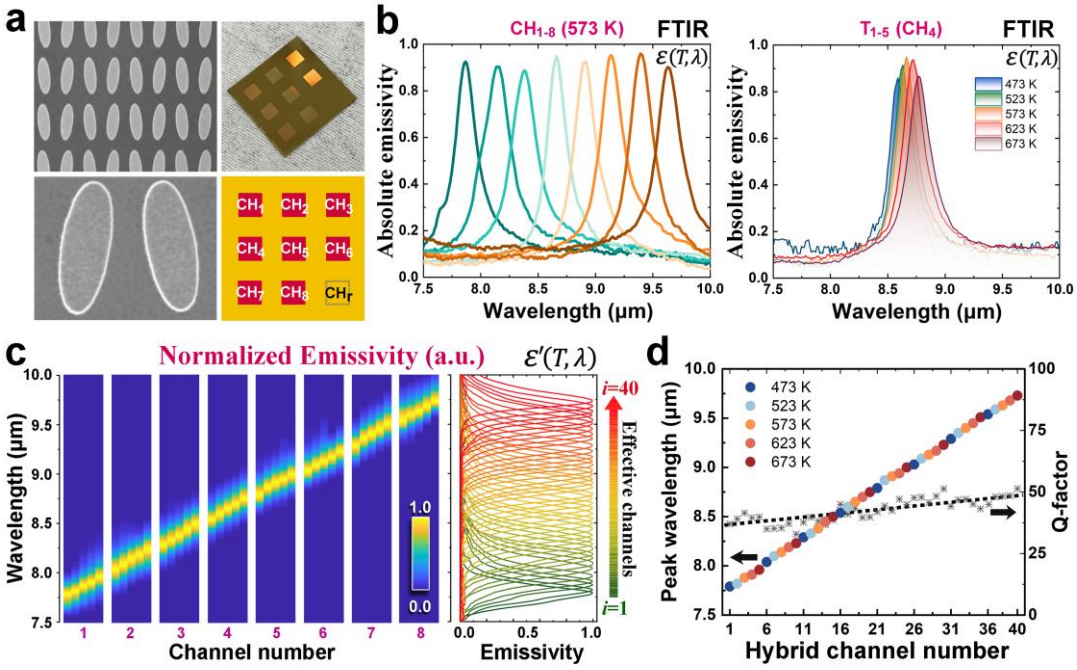


Figure 3. Experimental characterization of q-BIC emitter arrays and FTIR-calibrated spectral library of the hybrid encoding channels. a, SEM image of the dual-ellipse Ge resonators, device photograph, and chip layout defining the eight spatial channels. b, Left: measured absolute emissivity of the eight spatial channels at 573 K. Right: measured emissivity of CH_4 at 473, 523, 573, 623, and 673 K. c, Relative emissivity spectra of the eight spatial channels at five temperature states. Note that normalization is applied for display purposes only. d, Statistical analysis of the center wavelengths and Q-factors of the 40 hybrid q-BIC states.

From Fig. 3b, the absolute emissivity spectra exhibit considerable background and noise, arising partly from the intrinsic difficulty of mid-infrared spectral detection, and partly from the superposition of environmental thermal radiation reflected by the q-BIC structure onto the active emission signal. To suppress such undesirable contributions to the thermal emission spectra, we introduce a relative emissivity defined as:

$$\varepsilon'_{CH_i}(\lambda) = \frac{L_{CH_i}(\lambda) - L_{CH_r}(\lambda)}{L_{BB}(\lambda) - L_{CH_r}(\lambda)}$$

where the target channel signal is differenced against the reference channel (CH_r) to subtract the background radiation from the q-BIC sample itself and other stray contributions in the system. This processing preserves the effective encoded spectral components for subsequent

reconstruction while avoiding spectral distortions from unknown interference sources. After this subtraction, the relative emissivity results of all 40 hybrid states are shown in Fig. 3c, where both the background level and noise are substantially suppressed. More importantly, through careful design and matching of the geometric and thermal tuning states, the 40 hybrid spectra maintain uniform distribution across the entire spectral range, with only a ~100 nm blue shift relative to the simulation results shown in Fig. 2g. The resonance peaks extracted from these 40 spectra exhibit excellent linearity with channel index (Fig. 3d). Across all hybrid states, the Q-factors remain consistently in the range of 40~50. It is worth emphasizing that the central goal of this work is to develop a spectral encoding and reconstruction technique compatible with uncooled thermal imaging. The signal-to-noise ratio of a low-cost, pixelated uncooled bolometer array is far inferior to that of a cooled single-element MCT detector. Although q-BIC designs can in principle achieve extremely high Q-factors by balancing radiative and ohmic losses (Supplementary Section S4), an excessively narrow linewidth drastically reduces the integrated signal over the camera's spectral response window (8–14 μm). As a result, both the off-resonance background and the reflected ambient radiation from the *q*-BIC structure would overwhelm the channel signal. In our preliminary comparison, when the thermal emission Q-factor exceeds 100, the uncooled camera can barely distinguish the *q*-BIC patterned region from the reference planar region, confirming that a moderate Q-factor in the range of 40–50 is a deliberate and necessary choice for practical uncooled imaging-based spectral encoding.

Miniaturized Spectrometer Integration and Spectral Reconstruction

With the calibrated spectral library of the 40 hybrid channels established, we integrated a miniaturized, low-cost MIR spectrometer system, as shown in Fig. 4a. The multi-channel thermal emission from the source chip is captured by an uncooled thermal camera and encoded into temperature signals, which can be read out in real time via a computer or even a mobile phone APP. However, in addition to the desired narrowband emission signals, thermal imaging inherently suffers from multiple, complex, and unwanted background contributions. Some contributions can be modeled using Planck's law, such as reflected ambient radiation and sample self-emission. Others, including internal stray radiation from the camera itself, are unpredictable. These unwanted contributions must be carefully subtracted. These unwanted contributions must be carefully subtracted to enable faithful spectral reconstruction via the CS model. To establish a reliable background-correction model for this purpose, we analyze the major signal contributions involved in the thermal imaging process, as illustrated in Fig. 4b. The spectral radiance of a blackbody at temperature T is given by Planck's law[36]:

$$M_{BB}(\lambda, T) = \frac{2\pi hc^2}{\lambda^5 \left[\exp\left(\frac{hc}{\lambda k_B T}\right) - 1\right]}$$

For the i-th encoding channel, the total spectral radiance received by the thermal camera can thus be expressed as:

$$L_i(\lambda) = \tau(\lambda)\varepsilon_i(\lambda)M_{BB}(\lambda, T_s) + \tau(\lambda)[1 - \varepsilon_i(\lambda)]M_{BB}(\lambda, T_a) + [1 - \tau(\lambda)]M_{BB}(\lambda, T_a)$$

where T_s and T_a are the source and ambient temperatures, respectively, and $\tau(\lambda)$ is the transmittance of the optical path, with $\tau = 1$ in the absence of the sample and $\tau(\lambda) = x(\lambda)$ when a sample is present (i.e., the target spectra for CS reconstruction). The camera then integrates this spectral radiance over its spectral response function $R(\lambda)$, yielding the measured signal for the i-th hybrid encoded channel:

$$V'_{CH_i} = \int R(\lambda)L_i(\lambda)d\lambda + V_{bg}$$

where V_{bg} accounts for all the uncalibrated background contributions and camera-specific offsets arising from internal electronics and image processing algorithms, which can be effectively eliminated by taking the difference between each encoded channel and the reference channel: $\Delta V'_{CH_i} = V'_{CH_i} - V'_{CH_r}$. To further remove the absolute intensity mismatch between the simulated and measured signals, we define a normalized ratio for measurements with and without the sample:

$$y'_i = \frac{\Delta V_{i,m}}{\Delta V_i} \approx \frac{\int w_i(\lambda)x(\lambda)d\lambda}{\int w_i(\lambda)d\lambda}$$

$$w_i(\lambda) = R(\lambda)\varepsilon'_i(\lambda)[M_{BB}(\lambda, T) - M_{BB}(\lambda, T_a)]$$

where $\varepsilon'_i(\lambda)$ denotes the relative emissivity of the i-th encoding state extracted from the FTIR measurements (Fig. 3c). Based on the above formulation, we now construct the CS model. The input measurement vector Y for CS is obtained by processing the raw thermal imaging data of each channel (V_{CHi}) using the same procedure described above, yielding $y_i = \Delta V_{i,m}/\Delta V_i$ for the i-th encoded channel. The target spectrum X is discretized over $j = 1, \ldots, 401$ wavelength points spanning 7.8–9.8 μm, which fully covers the emission bands for the 40 hybrid encoding states. The discrete form of the forward model $y_i = y'_i + \eta$ can thus be expressed as:

$$y_i \approx \sum_{j=1}^{401} \Phi_{ij}x_j + \eta$$

where $\Phi_{ij} = c \cdot w_i(\lambda_j)$ is the measurement matrix of our CS model. The above models provide the basis for subtracting the background contributions and extracting the sample-specific

absorption features from the encoded thermal images via the CS reconstruction algorithm. (see Supplementary Sections S5 and S6 for more details)).

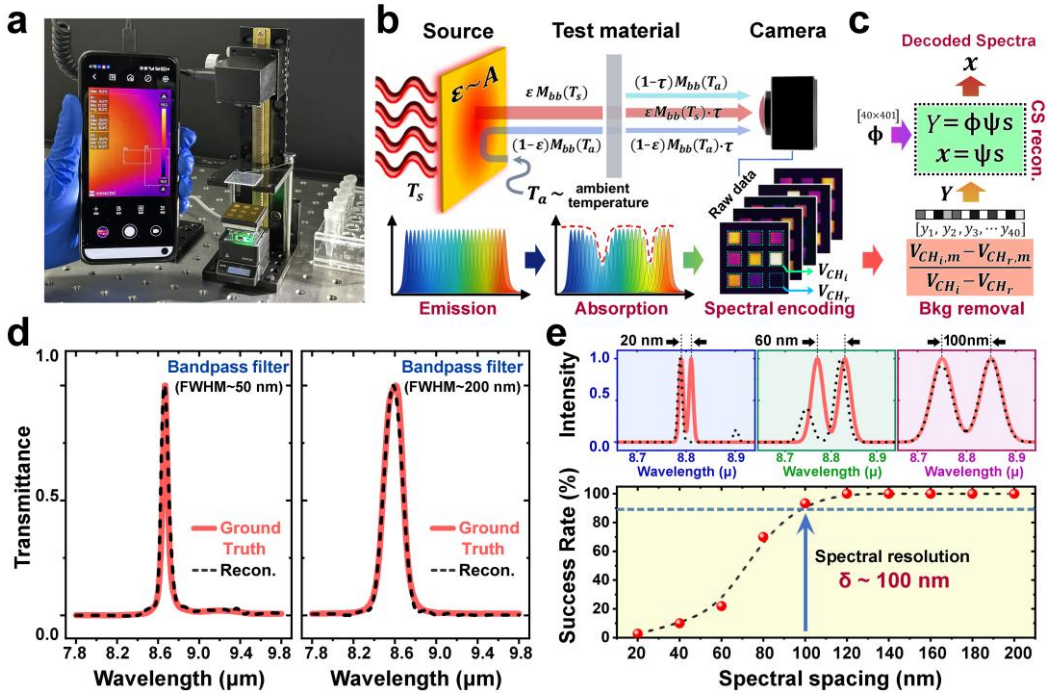


Figure 4. System integration, background correction, and spectral reconstruction. a, Photograph of the miniaturized MIR spectrometer system. b–c, Schematic of the signal contributions received by the thermal camera and the subsequent background-subtraction and CS reconstruction workflow. d, Reconstructed transmission spectra of bandpass filters with 50 nm and 200 nm linewidths, compared with FTIR references. e, Reconstruction of synthetic double-peak spectra with varying peak spacings (20–200 nm) and the corresponding success rate as a function of peak spacing (lower panel).

We validate the spectral reconstruction capability using three representative samples. To validate the spectral reconstruction capability of our system, we first tested two representative bandpass filters with linewidths of 50 nm and 200 nm. As shown in Fig. 4d, the reconstructed transmission spectra agree remarkably well with the FTIR references, accurately recovering the peak positions, spectral linewidths, and peak-to-background contrast with a fidelity exceeding 95% (see Supplementary Section S7 for the definition of fidelity). To further evaluate the spectral resolution of our system, we analyzed its ability to resolve double-peak features. Since mid-infrared test samples or devices with precisely controlled narrow peak separations are difficult to obtain experimentally, we constructed synthetic transmission spectra with varying peak-to-peak spacings as the ground truth. Using the FTIR-calibrated emissivity data as the measurement basis, we performed CS reconstructions on these synthetic spectra. To emulate realistic conditions, we added random noise to the simulated measurement vector Y according to the typical temperature measurement accuracy of the thermal camera (±2%). This semi-experimental approach ensures that the reconstruction results closely reflect practical performance. As shown in Fig. 4e, we evaluated the reconstruction fidelity for double-

peak spectra with spacings ranging from 20 nm to 200 nm. For a spacing of 20 nm, the reconstructed spectrum exhibits large deviations with considerable randomness. At 60 nm, the two peaks become discernible but their relative intensities are poorly recovered. In contrast, for a spacing of 100 nm, the reconstruction reproduces the input spectrum with high fidelity. To quantitatively assess the resolution limit, we introduced a success rate metric that is considerably more stringent than the spectral fidelity criterion (which already exceeds 95%). This metric comprehensively evaluates the agreement between the reconstructed and ground-truth spectra in terms of peak positions, intensity ratios, and spectral correlation (see Supplementary section S7 for detailed definition). As shown in the lower panel of Fig. 4e, the success rate remains low for spacings below 60 nm, then increases sharply as the spacing increases, exceeding 90% at 100 nm and approaching 100% for larger spacings. These results confirm that our spectrometer, based on only 40 hybrid encoding channels, can retrieve high-dimensional spectral information with excellent accuracy, achieving a spectral resolution below 100 nm (defined as the spacing at which the double-peak success rate exceeds 90%, with the actual reconstruction fidelity exceeding 95%), providing a solid foundation for subsequent practical applications.

Practical Spectroscopic Applications

Having validated the spectral reconstruction capability and resolution of our system, we now turn to its practical performance in real-world mid-infrared spectroscopic analysis. Unlike the well-defined bandpass filters or synthetic double-peak spectra used in the previous validation, actual material samples exhibit complex, closely spaced molecular fingerprint absorption bands with relatively low contrast. Reliably resolving such features is essential for practical applications, as it directly determines the system's utility in identifying and quantifying chemical substances. To this end, we conducted three representative experiments covering material identification, concentration quantification, and chemical process monitoring—each addressing a distinct yet practically relevant scenario in MIR spectroscopy.

We prepared seven common plastics (PP, PTFE, PVC, EVA, PI, PPS, and HDPE), each with five individual samples, resulting in a mixed pool of 35 randomly ordered samples. For each measurement, the reconstructed spectrum was compared against the FTIR reference libraries of the seven materials, and the label with the highest reconstruction fidelity was assigned as the identification result. As shown in Fig. 5a (left panel), the reconstructed spectra of all seven plastics agree remarkably well with their FTIR references, capturing most of the characteristic peak-and-valley features. The classification results are summarized in the

confusion matrix of Fig. 5a (right panel), where all 35 samples were correctly identified, yielding a 100% sorting success rate. We further explored quantitative detection using PMMA/anisole precursor solutions at concentrations ranging from 4% to 9%. After spin-coating and baking, the resulting PMMA films were measured by both our system and FTIR. As the precursor concentration increases, the characteristic absorption bands of PMMA exhibit a systematic enhancement (Fig. 5b, left panel). Using a partial least squares (PLS) calibration model established from FTIR spectra of standard concentrations, we predicted the concentrations of each sample. The statistical results in Fig. 5b (right panel) show excellent agreement with the true values, with a root-mean-square error (RMSE) as low as 0.086%, demonstrating the system's high accuracy in quantitative analysis (see Supplementary Information Sections S8 for more details).

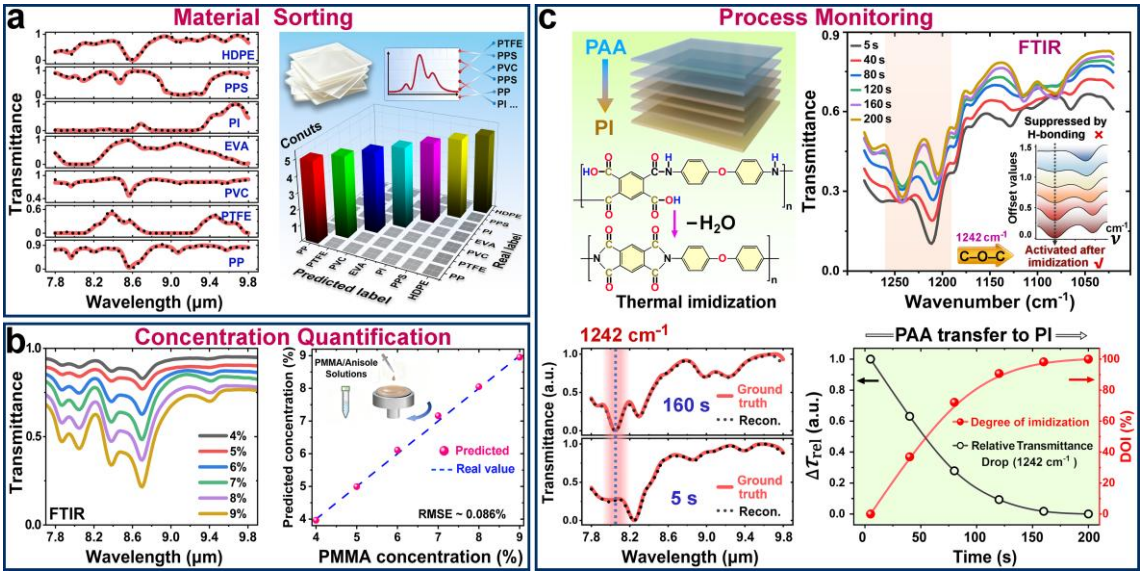


Figure 5. Practical spectroscopic applications. a, Material sorting of seven plastics. Left: reconstructed transmission spectra compared with FTIR references. Right: confusion matrix showing classification results. b, Concentration quantification of PMMA films (4–9%). Left: reconstructed spectra with increasing concentration. Right: predicted versus true concentrations. c, Process monitoring of PAA-to-PI thermal imidization. Upper: molecular structural transformation from PAA to PI and corresponding FTIR spectra evolution. Lower: reconstructed spectra compared with FTIR references and analysis of the imidization degree through the C–O–C absorption feature at 1242 cm^{-1}.

In industrial material synthesis and process development, in-situ monitoring of chemical reactions is of critical importance, as the formation and consumption of specific molecular bonds at different stages directly reflect the reaction progress. Therefore, we further demonstrate the system‘s utility in process monitoring by tracking the thermal imidization of polyamic acid (PAA) to polyimide (PI) on ZnS substrates at 180 °C for durations ranging from 5 s to 200 s (see Supplementary Sections S9 for more details on sample preparation). The left panel of Fig. 5c illustrates the molecular structural transformation from PAA to PI via intramolecular dehydration cyclization, while the right panel shows the corresponding FTIR

spectra. In the stacked FTIR spectra near the 1250–1200 cm^{-1} region, we observe a significant overall rise in transmittance at ~1211 cm^{-1} as heating proceeds; however, this rise is primarily attributed to solvent evaporation, as evidenced by the minimal change in the normalized spectral intensity at this wavenumber. In contrast, a distinct absorption dip gradually emerges at ~1242 cm^{-1} during heating. This band is assigned to the C–O–C stretching vibration of the aromatic ether moiety [37]. In the PAA precursor, this absorption is suppressed by the extensive hydrogen-bonding network formed between the carboxyl and amide groups. Upon thermal imidization, the dehydration cyclization consumes these groups, disrupting the hydrogen bonds and rigidifying the polymer backbone, which activates the C–O–C vibration and leads to the progressive appearance and enhancement of the 1242 cm^{-1} dip. The reconstructed spectra from our system (bottom left) reproduce the FTIR references with high fidelity across the entire wavelength range. To quantify the imidization progress and exclude solvent-induced artifacts, we define the degree of imidization as DOI = $1 - \Delta\tau_{rel}$, where $\Delta\tau_{rel}$ is the relative transmittance drop at 1242 cm^{-1} against the non-absorbing baseline (1262 cm^{-1}). As shown in the bottom-right panel, the DOI increases monotonically with heating time and saturates after approximately 200 s, confirming the capability of our system for real-time monitoring of molecular bond evolution during chemical processes.

Conclusion

In summary, we have developed a miniaturized mid-infrared spectrometer that bridges two long-standing yet disconnected domains. On one side, narrowband thermal emission engineering has been extensively studied over the past two decades, yet remains confined to cryogenic FTIR characterization. On the other, uncooled microbolometer detection offers low-cost and compactness, but struggles with narrowband spectral readout due to its large acceptance angle and complex background radiation. Our work resolves this incompatibility by establishing a source-side spectral manipulation architecture that fully embraces the characteristics of uncooled thermal imaging: we construct a rigorous background-subtraction and spectral reconstruction model that decodes the narrowband thermal emission from *q*-BIC metasurfaces directly from thermal image frames, achieving high-fidelity spectral retrieval without cooling or bulky optics. Complementing this system-level innovation, we introduce a hybrid encoding scheme that combines geometric tuning with thermo-optic tuning, expanding the effective channel count from eight physical channels to forty across the 7.5–10 μm band with a spectral resolution below 100 nm. Beyond these demonstrations, our approach offers a practical and cost-effective pathway toward field-deployable MIR spectroscopy, with the

added advantage that the hybrid encoding scheme is inherently scalable to densely packed spectral imaging arrays. By combining the rich molecular fingerprint information of the mid-infrared with compact, uncooled detection, this work opens a viable route for translating MIR spectroscopic analysis from laboratory benchtops into on-site environmental, clinical, and industrial applications where size, cost, and speed are paramount.

Methods

Numerical simulation

All numerical simulations were performed using the finite-element method in COMSOL Multiphysics 6.3. Floquet periodic boundary conditions were applied in the lateral directions of the unit cell to model the periodic array and define the incident wavevector. Perfectly matched layers were used in the z direction to simulate non-reflecting open boundaries. For angle-resolved simulations, the reflection, absorption, and emission responses at various angles were obtained by varying the transverse wavevector or the incident angle. Since the Au back-reflector suppresses transmission, the absorption was approximated by $A = 1 - R$, and the thermal emission spectra were derived accordingly via Kirchhoff's law.

Device fabrication

The fabrication process involved metal reflector deposition, dielectric spacer and Ge film deposition, electron-beam lithography (EBL), hard-mask transfer, ICP-RIE etching, and mask removal. First, 5 nm Ti and 120 nm Au were deposited onto a Si substrate by electron-beam evaporation, followed by 500 nm ZnS and 700 nm Ge. PMMA 950 A4 was spin-coated at 4000 rpm for 60 s and baked at 180 °C for 90 s. The patterns were exposed using a 100 kV EBL system, developed in MIBK:IPA = 1:3 for 120 s, and rinsed in IPA for 30 s. A 30 nm Al_2O_3 hard mask layer was then deposited by e-beam evaporation. The Al_2O_3 pattern was formed by lift-off, and the Ge layer was etched using an Oxford Instruments Plasma Pro 100 Cobra ICP-RIE system. The residual Al_2O_3 hard mask was removed by 2.38% TMAH for 60 s.

Camera-based coded thermal-frame acquisition

The thermal images were acquired using an uncooled microbolometer thermal camera (HIKMICRO P20MAX) with a frame interval of approximately 40 ms and an imaging working distance of about 10 cm, ensuring clear imaging of each spectral channel. The Mini-heater was set to temperatures of 200 °C, 250 °C, 300 °C, 350 °C, and 400 °C. The raw temperature data were extracted from the thermal images output by the camera to encode each spectral channel. All measurements were performed at room temperature. In addition, an 8–12 μm bandpass filter and a wire-grid polarizer were placed in the optical path to ensure sufficient signal-to-noise ratio of our spectral encoding purpose.

Acknowledgments

We acknowledge financial supports from National Natural Science Foundation of China (Nos. 62220106001, 12374351), Key-Area Research and Development Program of Guangdong Province (No. 2023B0101200009) and the open project of the Key Lab of Advanced Optical Manufacturing Technologies of Jiangsu Province, Soochow University (KJS2333).

Author contributions

L.W., Q.C. and B.L. conceived the idea and designed the experiments. Q.L., Y.W. and Z.X. fabricated the q-BIC chip and performed the FTIR and thermal imaging measurements. Q.L. performed all optical simulations and design. Y.L., Y.H. and Y.Z. established the spectral encoding and decoding model and algorithm, and completed the spectral reconstruction. All authors discussed the results and contributed to the preparation of the manuscript.

Data availability

All of the data required to evaluate the conclusions of this study are presented within the article or its Supplementary Information or are available on request from the corresponding authors.

Competing interests

The authors declare no competing financial interests.

References

1. Barrios, V. A. E., Mendez, J. R. R., Aguilar, N. V. P., Espinosa, G. A. & Rodriguez, J. L. D. in *Infrared Spectroscopy* (ed. Theophile, T.) (InTech, 2012).
2. Cozzolino, D. (ed.) *Infrared Spectroscopy: Theory, Developments and Applications* (Nova Science Publishers, 2022).
3. Griffiths, P. R. Fourier transform infrared spectrometry. *Science* **222**, 297–302 (1983).
4. Dinh, T.-V., Choi, I.-Y., Son, Y.-S. & Kim, J.-C. A review on non-dispersive infrared gas sensors: Improvement of sensor detection limit and interference correction. *Sens. Actuators B Chem.* **231**, 529–538 (2016).
5. Sun, J., Chang, J., Wang, C. & Shao, J. Tunable diode laser absorption spectroscopy for detection of multi-component gas: a review. *Appl. Spectrosc. Rev.* **59**, 1086–1107 (2024).
6. Mitra, C. Mid-Infrared Spectroscopy and Challenges in Industrial Environment. in *Infrared Spectroscopy - Principles, Advances, and Applications* (ed. El-Azazy, M.) (IntechOpen, 2019).
7. Zhang, Z., Xiao, S., Song, Q. & Xu, K. Scalable on-chip diffractive speckle spectrometer with high spectral channel density. *Light Sci. Appl.* **14**, 130 (2025).
8. Yang, J. W., Cui, K. Y., Huang, Y. D. et al. Ultraspectral imaging based on metasurfaces with freeform shaped meta-atoms. *Laser Photonics Rev.* **16**, 2100663 (2022).
9. Zhang, W., Suo, J., Dong, K., Li, L., Yuan, X., Pei, C. & Dai, Q. Handheld snapshot multi-spectral camera at tens-of-megapixel resolution. *Nat. Commun.* **14**, 5043 (2023).
10. Liang, W., Nan, X., Cai, W. et al. Single-pixel infrared miniaturized spectrometer enabled by ultra-broadband reconfigurable photodetection. *Adv. Sci.* **12**, 2500830 (2025).
11. Zheng, Q., Nan, X., Chen, B. et al. On-chip near-infrared spectral sensing with minimal plasmon-modulated channels. *Laser Photonics Rev.* **17**, 2300475 (2023).
12. Wang, A. & Dan, Y. Mid-infrared plasmonic multispectral filters. *Sci. Rep.* **8**, 11257 (2018).

13. Qu, Y., Zhou, Q., Xiang, J. & Yu, Z. Sparsity for ultrafast material identification. *Laser Photonics Rev.* **18**, 2300069 (2024).
14. Tan, H., Meng, J. & Crozier, K. B. Multianalyte detection with metasurface-based mid-infrared microspectrometer. *ACS Sens.* **9**, 5839–5847 (2024).
15. Meng, J., Weston, L., Balendhran, S., Wen, D., Cadusch, J. J., Unnithan, R. R. & Crozier, K. B. Compact chemical identifier based on plasmonic metasurface integrated with microbolometer array. *Laser Photonics Rev.* **16**, 2100436 (2022).
16. Nagao, T., Thang, D. D., Anh, D. T., Ishii, S. & Nabatame, T. Wavelength-selective photothermal infrared sensors. in *System-Materials Nanoarchitectonics* (eds. Wakayama, Y. & Ariga, K.) (NIMS Monographs, Springer, 2022).
17. Litke, A., Zakizade, E., Michel, M., Weyers, S. & Schall-Giesecke, A. L. Plasmonic metamaterial absorber for MWIR and LWIR bispectral microbolometers. *Micro Nano Eng.* **23**, 100262 (2024).
18. Tan, X., Zhang, H., Li, J., Wan, H., Guo, Q., Zhu, H., Liu, H. & Yi, F. Non-dispersive infrared multi-gas sensing via nanoantenna integrated narrowband detectors. *Nat. Commun.* **11**, 5245 (2020).
19. Chen, Q., Liang, L., Zheng, Q., Zhang, Y. & Wen, L. On-chip readout plasmonic mid-IR gas sensor. *Opto-Electron. Adv.* **3**, 190040 (2020).
20. Chu, Q. Q., Zhang, F., Zhang, Y., Zhu, S. N. & Liu, H. Indirect measurement of infrared absorption spectrum through thermal emission of meta-cavity array. *Opt. Express* **31**, 39832–39840 (2023).
21. Chen, Q., Nie, H., Liu, Q. K., Tan, N., Tuo, Z. W., Yan, J. H. & Wen, L. Metasurface-engineered thermal emitters enabled chip-scale mid-infrared spectroscopic sensing. *Photonix* **6**, 19 (2025).
22. Baranov, D. G., Xiao, Y., Nechepurenko, I. A., Krasnok, A. E., Alù, A. & Kats, M. A. Nanophotonic engineering of far-field thermal emitters. *Nat. Mater.* **18**, 920–930 (2019).
23. Li, W. & Fan, S. Nanophotonic control of thermal radiation for energy applications [Invited]. *Opt. Express* **26**, 15995–16021 (2018).
24. Chu, Q. Q., Zhong, F., Shang, X. H., Zhang, Y., Zhu, S. N. & Liu, H. Controlling thermal emission with metasurfaces and its applications. *Nanophotonics* **13**, 1279–1301 (2024).
25. Zhang, Y. R. & Zhang, M. M. Coherent control of thermal radiation with nanophotonics. *Adv. Photonics Res.* **6**, 2500019 (2025).
26. Greffet, J.-J., Carminati, R., Joulain, K., Mulet, J.-P., Mainguy, S. & Chen, Y. Coherent emission of light by thermal sources. *Nature* **416**, 61–64 (2002).
27. Arnold, C., Marquier, F., Garin, M., Pardo, F., Collin, S., Bardou, N., Pelouard, J.-L. & Greffet, J.-J. Coherent thermal infrared emission by two-dimensional silicon carbide gratings. *Phys. Rev. B* **86**, 035316 (2012).
28. Carminati, R. & Greffet, J.-J. Near-field effects in spatial coherence of thermal sources. *Phys. Rev. Lett.* **82**, 1660–1663 (1999).
29. Laroche, M., Arnold, C., Marquier, F., Carminati, R. & Greffet, J.-J. Highly directional radiation generated by a tungsten thermal source. *Opt. Lett.* **30**, 2623–2625 (2005).

30. Liu, X. X., Li, Z., Wen, Z., Wu, M., Lu, J., Chen, X., Zhao, X., Wang, T., Ji, R., Zhang, Y., Sun, L., Zhang, B., Xu, H., Zhou, J., Hao, J. & Wang, L. Large-area, lithography-free, narrow-band and highly directional thermal emitter. *Nanoscale* **11**, 19742–19750 (2019).
31. Yang, Z.-Y., Ishii, S., Yokoyama, T., Dao, T. D., Sun, M.-G., Pankin, P. S., Timofeev, I. V., Nagao, T. & Chen, K.-P. Narrowband wavelength selective thermal emitters by confined Tamm plasmon polaritons. *ACS Photonics* **4**, 2212–2219 (2017).
32. Sun, K., Cai, Y., Huang, L. & Han, Z. Ultra-narrowband and rainbow-free mid-infrared thermal emitters enabled by a flat band design in distorted photonic lattices. *Nat. Commun.* **15**, 4019 (2024).
33. Yang, S., He, M., Hong, C., Nordlander, J., Maria, J.-P., Caldwell, J. D. & Ndukaife, J. C. Single-peak and narrow-band mid-infrared thermal emitters driven by mirror-coupled plasmonic quasi-BIC metasurfaces. *Optica* **11**, 305–314 (2024).
34. Tao, Z. F., He, Y. F., Sun, S. L., Zhou, C. F. & Zhou, Z. P. Narrowband mid-infrared thermal emitters based on the Fabry–Perot type of bound states in the continuum. *Opt. Express* **31**, 20338–20344 (2023).
35. Li, H. Refractive index of silicon and germanium and its wavelength and temperature derivatives. *J. Phys. Chem. Ref. Data* **9**, 561–658 (1993).
36. Planck, M. On the law of distribution of energy in the normal spectrum. *Ann. Phys.* **4**, 553–563 (1901).
37. Kim, M. J. et al. Photoluminescence, thermal and surface properties of triarylimidazole-containing polyimide nanocomposite films. *Polymers* **13**, 377 (2021).

Supplementary Files

This is a list of supplementary files associated with this preprint. Click to download.

- SupplementaryMaterial.docx